Electrochemistry

Deutsche Ausgabe: DOI: 10.1002/ange.201500133
Internationale Ausgabe: DOI: 10.1002/anie.201500133

Extraordinary Supercapacitor Performance of a Multicomponent and Mixed-Valence Oxyhydroxide**

*Jianli Kang, Akihiko Hirata, Luyang Chen, Shengli Zhu, Takeshi Fujita, and Mingwei Chen**

Abstract: *We report a novel multicomponent mixed-valence oxyhydroxide-based electrode synthesized by electrochemical polarization of a de-alloyed nanoporous NiCuMn alloy. The multicomponent oxyhydroxide has a high specific capacitance larger than 627 F cm^{-3} (1097 ± 95 F g^{-1}) at a current density of 0.25 A cm^{-3}, originating from multiple redox reactions. More importantly, the oxyhydroxide electrode possesses an extraordinarily wide working-potential window of 1.8 V in an aqueous electrolyte, which far exceeds the theoretically stable window of water. The realization of both high specific capacitance and high working-potential windows gives rise to a high energy density, 51 mWh cm^{-3}, of the multicomponent oxyhydroxide-based supercapacitor for high-energy and high-power applications.*

Despite the fact that a large number of new materials have recently been developed for high-energy-density supercapacitors, they usually suffer from a low specific capacitance and/or a narrow working potential window.[1] The energy density (E) of an electrochemical supercapacitor is determined by the specific capacitance (C) and the stable working-potential window (V) of an electrode material through the equation: $E = 0.5\,CV^2$. For most active electrode materials, the efficient electrochemical potential window is usually no more than 1.23 V in aqueous electrolytes, which is restricted by the thermodynamic potential of water electrolysis.[2] Although nonaqueous electrolytes can provide a wide potential window, the specific capacitance of active materials, particularly pseudocapacitive materials, in nonaqueous electrolytes is often much lower than that in aqueous ones.[3] Therefore, developing new electrode materials with both high specific capacitance and a wide working-potential window is crucial for the new generation of supercapacitors that have a high energy density along with high specific power and fast charging/discharging rate to complement or even surpass batteries for high-energy and high-power applications.[1b] Herein, we report that Cu and Mn cation co-doping gives rise to the synergetic effect in enhanced specific capacitance of Ni hydroxide by introducing multiple redox reactions and in enlarged working-potential windows in aqueous solutions. The resultant multicomponent and mixed-valence oxyhydroxide ($Ni^{II}_aCu^{I}_bCu^{II}_cMn^{II}_dMn^{IV}_e)O_f(OH)_g{\cdot}hH_2O$ (abbreviated to NiCuMnOOH, hereinafter) shows ultrahigh specific capacitance of about 627 F cm^{-3} (1097 ± 95 F g^{-1}) at a current density of 0.25 A cm^{-3} and a large operating potential window of 1.8 V in an aqueous electrolyte.

The fabrication process of the multicomponent NiCuMnOOH oxyhydroxide was illustrated in Figure 1a. Single-phase $Ni_{15}Cu_{15}Mn_{70}$ (at. %) alloy ribbons with a thickness of ca. 20 μm were electrochemically de-alloyed in 1 M $(NH_4)_2SO_4$ solution at −0.7 V (vs. Ag/AgCl) to form a nanoporous $Ni_{36.5}Cu_{36.5}Mn_{27}$ ternary alloy by partially leaching less stable Mn.[4] X-ray diffraction (XRD) reveals that the nanoporous alloy has a monolithic face-centered cubic (FCC) structure (Figure 1b). The mean ligament size, calculated from the full width at half maximum (FWHM) of the XRD pattern according to the Debye–Scherrer equation, is ca. 5.2 nm. The nanoporous $Ni_{36.5}Cu_{36.5}Mn_{27}$ alloy was further polarized in 1 M KOH solution at 0.9 V to oxidize the ternary alloy.[4b] After the formation of a stable oxide layer, the metal ligament size was reduced to about 3.4 nm whereas the thickness of the ribbons remained to be ca. 20 μm. As shown in the scanning transmission electron microscope (STEM) image (Figure 1c), the nanopore channels are almost filled by a leaky polarization product with pore sizes smaller than 1 nm.

The Brunauer–Emmett–Teller measurement also confirmed that small pores with a size of ca. 0.59 nm are formed by the polarization (Figure S1). The selected area electron diffraction (SAED) pattern (the inset of Figure 1c) demonstrates that only two crystalline phases, that is, the hydroxide with a cubic structure and the residual FCC metal substrate, can be detected from the polarized nanoporous alloy. The hydroxide has a coherent crystallographic relationship with the residual Ni-rich substrate. The two phases with different lattice constants and contrast can be identified from a high-angle annular dark field (HAADF) STEM image (Figure 1d). The inverse fast Fourier transform (FFT) micrograph of Figure 1d, which is constructed by imaging each phase using the representative FFT patterns of the hydroxide and metal,

[*] Dr. J. L. Kang
School of Materials Science and Engineering and State Key Laboratory of Separation Membranes and Membrane Processes
Tianjin Polytechnic University
Tianjin 300387 (China)
Dr. J. L. Kang, A. Hirata, L. Y. Chen, S. L. Zhu, T. Fujita, Prof. M. W. Chen
WPI Advanced Institute for Materials Research, Tohoku University
Sendai 980-8577 (Japan)
E-mail: mwchen@wpi-aimr.tohoku.ac.jp
Prof. M. W. Chen
CREST (Japan) Science and Technology Agency (JST)
Saitama 332-0012 (Japan)
Prof. M. W. Chen
State Key Laboratory of Metal Matrix Composites, School of Materials Science and Engineering, Shanghai Jiao Tong University
Shanghai 200030 (China)

[**] This work was sponsored by JST-CREST "Phase Interface Science for Highly Efficient Energy Utilization", MEXT (Japan).

Supporting information for this article is available on the WWW under http://dx.doi.org/10.1002/anie.201500133.

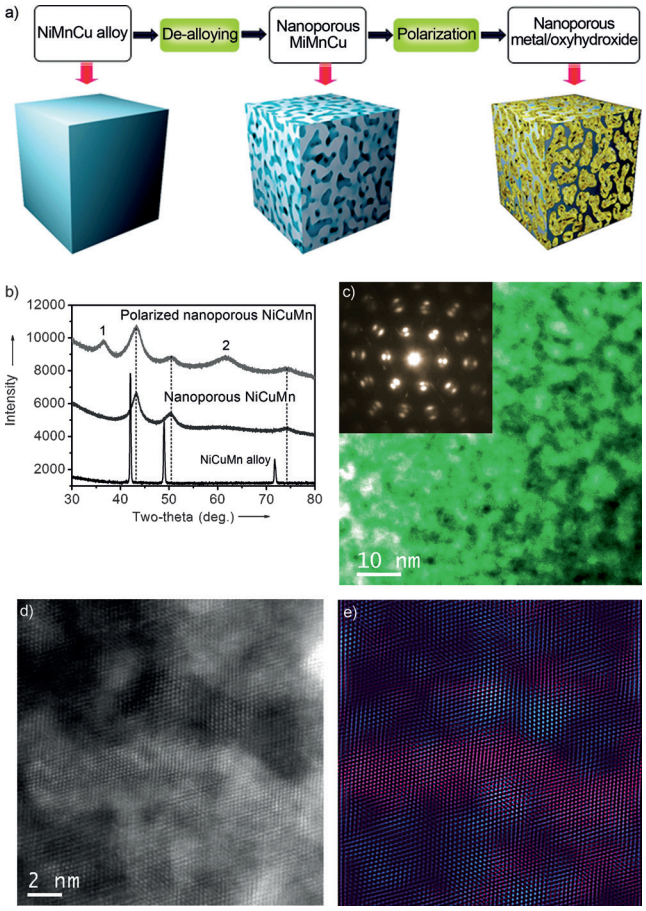

Figure 1. a) Illustration of the fabrication process of the oxyhydroxide supported by interconnected metal skeletons; b) XRD spectra of the precursor NiCuMn alloy, de-alloyed nanoporous NiCuMn, and electrochemically polarized nanoporous NiCuMn. c) STEM micrograph of the electrochemically polarized nanoporous NiCuMn alloy. The inset is the SAED pattern. d) HAADF-STEM image of the polarized nanoporous NiCuMn. The contrast variation in the atomic-resolution image originates from the mass difference between the metal skeletons and oxyhydroxide filler as well as the hierarchical nanoporosity. e) The inverse FFT image of (d) showing the distribution of oxyhydroxide (blue) and metal skeletons (violett).

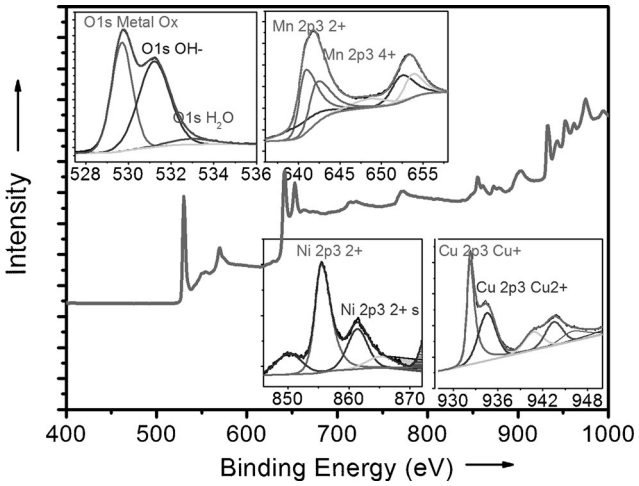

Figure 2. XPS spectra of the $(Ni^{II}_{a}Cu^{I}_{b}Cu^{II}_{c}Mn^{II}_{d}Mn^{IV}_{e})O_{f}(OH)_{g}\cdot h\,H_2O$ oxyhydroxide. The insets are high-resolution spectra for individual elements of the Ni 2p, Mn 2p, Cu 2p, and O 1s orbitals.

shows the distribution of the hydroxide and the residual metal substrate (Figure 1e). The volume fraction of the porous oxide phase is approximately 60–70%, which is fully confined within the nanopore channels of the residual nanoporous alloy that has an open three-dimensional porous structure.

The microstructure of the polarized sample was further characterized by XRD. As shown in Figure 1b, two weak and broad peaks at 36.5° and 61.6° appear after the polarization, which can be indexed as the (111) and (220) peaks of a rock-salt-type oxide with the lattice constant of about 0.426 nm, just between those of the known rock-salt-type oxides, MnO (0.445 nm) and NiO (0.418 nm). Considering the nanoporous precursor is comprised of three elements, Cu, Ni, and Mn, the single-phase hydroxide most likely contains multiple metal cations, which leads to the large deviation in the lattice constant from pure MnO and NiO. To determine the chemical composition and valence state of the hydroxide phase, X-ray photoelectron spectroscopy (XPS) was employed to investigate the polarized sample. Mn 2p, Ni 2p, Cu 2p, and O 1s peaks can be detected (Figure 2 and Table S1) whereas the low-binding-energy peaks corresponding to the metallic states of Mn, Ni, and Cu cannot be found. It indicates that the polarized nanoporous alloy is fully covered by the hydroxide with a considerable volume fraction. As shown in the insets of Figure 2, the high-resolution XPS spectra reveal that the Mn 2p, Ni 2p, and Cu 2p peaks consist of divalent and tetravalent Mn ions, divalent Ni ions, and univalent and divalent Cu ions, respectively. In the O 1s spectrum, two evident binding energy peaks at 529.5 eV and 531.3 eV as well as a weak shoulder peak at 533.1 eV are the characteristic bands of oxygen in metal oxides (metal-O-metal), hydroxides (metal-OH) and bound water, respectively. Combined with TEM and XRD measurements, the hydroxide is determined to be a single-phase multicomponent mixed-valence NiCuMnOOH oxyhydroxide with a rock salt structure. The fractions of the constituent ions in NiCuMnOOH are listed in Table S1, which are estimated according to the integrated areas under each deconvoluted peak in the XPS spectra. Compared with the nanoporous $Ni_{36.5}Cu_{36.5}Mn_{27}$ precursor, the concentration of Mn in the oxide increases obviously, inferring that Mn is preferentially oxidized to form the Mn-rich oxyhydroxide during the polarization process.

A three-electrode system was used to assess the electrochemical properties of the nanoporous oxyhydroxide-based electrode. Figure 3a shows the cyclic voltammogram (CV) curves of the electrode with different potential windows in 1 M KOH electrolyte at a scan rate of 50 $mV\,s^{-1}$. The oxyhydroxide exhibits multiple redox peaks during CV scans. The most significant redox peaks appear at the potentials from 0.11 V to 0.47 V, which are very similar to those of NiO.[5] However, the other redox reactions of the oxyhydroxide electrode are not in full agreement with those of monolithic Cu and Mn oxides.[6] When the potential window extends to −1.15 V, except for the kinetically reversible redox peaks, no obvious increase of a cathodic current can be seen, suggesting

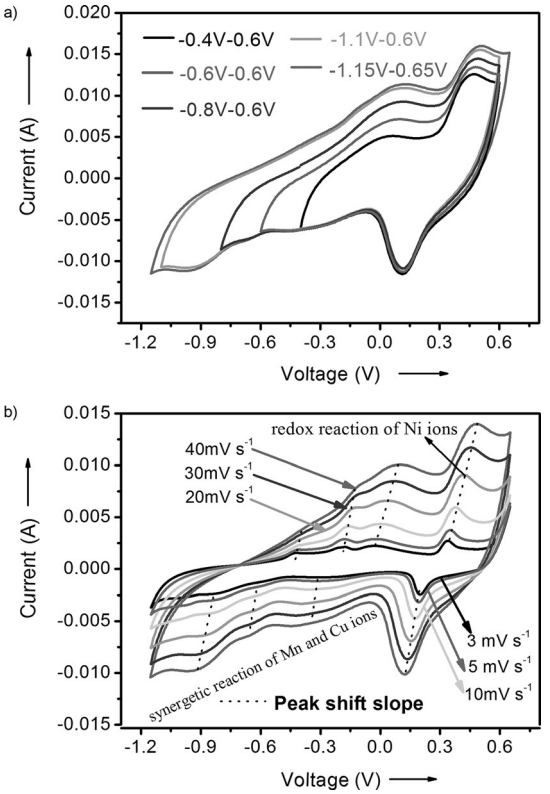

Figure 3. Electrochemical performance of the oxyhydroxide-based electrode tested by a three-electrode system in 1 M KOH electrolyte. a) Cyclic voltammograms with different potential windows at a scan rate of 50 $mV s^{-1}$; and b) cyclic voltammograms versus scan rates ranging from 3 to 40 $mV s^{-1}$.

that the multicomponent oxyhydroxide electrode is very stable against the irreversible reduction reaction of the oxyhydroxide and the hydrogen evolution reaction of the aqueous electrolyte. Therefore, the oxyhydroxide is electrochemically stable in an large potential window from −1.15 V to 0.65 V in the aqueous solution, which far exceeds the theoretically stable window of water.[3]

It is known that the effective working-potential window of oxides or oxyhydroxides of Ni, Mn, or Cu is usually no more than 1.0 V in aqueous electrolytes[5–7] and the mixture of Mn and Ni oxides can only slightly increase the potential window to 1.1 V.[8a] To understand the unusual working potential of the multicomponent oxyhydroxide in the alkaline solution, we investigated the electrochemical performances of polarized Ni film, nanoporous NiMn and CuMn binary alloys. As shown in Figure S2a, with the Ni hydroxide electrode, the alkaline electrolyte is stable in a wide potential range from −1.1 V to 0.6 V, because of the extra energy requirements for both cathode and anode reactions from Ohmic loss and the overpotential to obtain a required current density. This is consistent with the practical potential for effective alkaline water electrolysis of ca. 1.8–2.0 V at high current-density values of about 1000–3000 $A m^{-2}$ [8b] However, for the Ni hydroxide, there is no obvious redox reactions at potentials below 0.1 V and thus the effective potential window of the polarized Ni film is only ca. 0.5 V, similar to previous reports of Ni hydroxides.[5] Mn doping can extend the effective potential window to about 1.0 V (from −0.4 to 0.6 V) by introducing the reversible redox reactions in the cathodic region down to ca. −0.4 V. However, when the cathodic potential is lower than −0.1 V, the binary oxyhydroxide NiMnOOH is electrochemically unstable. After several tens of cycles, the CV curves mainly present the characteristic redox peaks of $Ni(OH)_2$ (Figure S2b). Meanwhile, the Mn cation redox peaks gradually disappear and the color of the electrolyte changes to yellow, indicating that irreversible dissolution or reduction of Mn cations takes place at low cathodic potentials, similar to that of V_2O_5.[9] For the multicomponent NiCuMnOOH oxyhydroxide, the Cu doping gives rise to an additional redox reaction of Cu cations in the cathodic region down to about −1.15 V and, meanwhile, the Cu cations stabilize the oxyhydroxide by preventing the irreversible dissolution of Mn cations (Figure S2c). The improved stable potential window from −1.1 V to 0.6 V for the pure Ni hydroxide to −1.15 V to 0.65 V of NiCuMnOOH is most likely due to the increase of the overpotentials for both cathode and anode reactions, caused by Cu and Mn doping, because detectable internal resistance changes cannot be seen in the electrochemical impedance spectra (Figure 4d). Therefore, it is reasonable to conclude that the

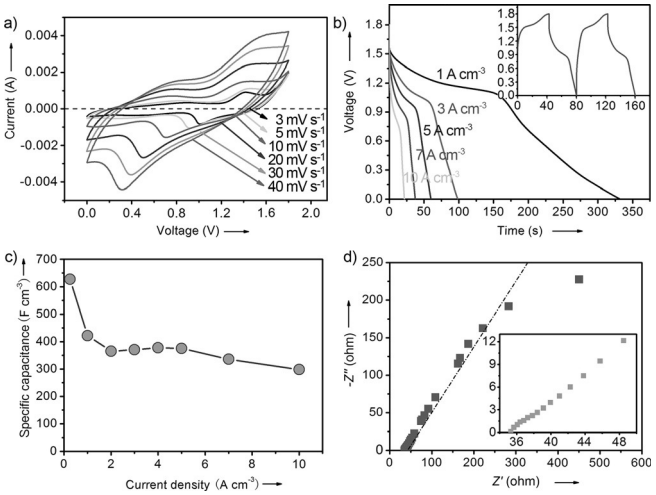

Figure 4. Supercapacitor performance of the oxyhydroxide electrode tested by a two-electrode configuration in 1 M KOH electrolyte. a) Cyclic voltammograms at scan rates from 3 to 40 $mV s^{-1}$. b) Discharge curves at different current densities. The inset shows typical charge/discharge curves. c) The specific volumetric capacitances of the electrode versus current density. d) Nyquist diagram of electrochemical impedance spectroscopy of the oxyhydroxide-based supercapacitor device. The inset is the enlarged high-frequency region.

large working potential window of NiCuMnOOH is mainly from the introduction and stabilization of the effective redox reactions in the cathodic potential region by the synergetic alloying effect of Ni, Cu, and Mn ions. Figure 3b shows the CV curves of the multicomponent oxyhydroxide electrode at different scan rates. With the scan rate increasing, all the oxidation peaks shift to higher potentials whereas the reduction peaks shift to lower potentials, indicating that the

redox reactions for charge storage are the diffusion-controlling process, same as that of monolithic Ni and Cu oxides and hydroxides, such as $Ni(OH)_2$, CuO, and NiO.[5,6a,11] To quantify the capacitive and diffusion-limited contributions to the total capacitance, we plotted the dependence of the diffusion-limited contribution on scan rates (Figure S3).[12] Although the diffusion-limited contribution is more evident at lower scan rates, the overall electrochemical performance of the multicomponent oxyhydroxide is dominated by the capacitive behavior.

The supercapacitor performance of the multicomponent oxyhydroxide-based electrode was investigated by using a symmetrical two-electrode device with 1M KOH as the electrolyte. The CV curves are shown in Figure 4a, confirming that the redox reactions are fully reversible. The charge/discharge curves exhibit obvious plateaus (Figure 4b), corresponding to the redox peaks in the CV curves. The volumetric capacitance of the electrode is measured by the CV and charge/discharge testing (Figures S4 and 4c). The volume for the specific capacitance calculations is based on the entire electrode, including the active oxyhydroxide, inactive metallic skeletons and open nanopores. The maximum volumetric capacitance is measured to be ca. 627 $F\,cm^{-3}$ at a low current density of 0.25 $A\,cm^{-3}$ (Figure 4c), which is among the best values achieved in supercapacitors so far[1,14,15] and ca. 4–12 times higher than the best reported values obtained with carbon materials[1b,f] and other high-performance pseudocapacitive composites.[13] Importantly, the high capacitive performance is obtained from 20 μm thick electrodes, which is different from most pseudocapacitive materials for which a high specific capacitance can only be realized from thin films. With the increase of current density, the volumetric capacitance gradually decreases due to the low utilization efficiency of the active oxyhydroxide at high charge/discharge currents. However, the specific capacitance still remains as high as about 300 $F\,cm^{-3}$ at the highest current density of 10 $A\,cm^{-3}$ in this study. To evaluate the specific mass capacitance of the pure multicomponent oxyhydroxide for comparison with other advanced pseudocapacitive materials, the mass of the oxyhydroxide in the nanoporous electrode is estimated to be ca. $0.57 \pm 0.05\ g\,cm^{-3}$ on the basis of EDS and XPS measurements (Figures S5 and S6). The specific mass capacitance of the oxyhydroxide is approximately $1097 \pm 95\ F\,g^{-1}$, comparable to the theoretical capacitance of RuO_2 (1300–1500 $F\,g^{-1}$)[16] and MnO_2 ($\approx 1370\ F\,g^{-1}$).[1g,17] The multicomponent oxyhydroxide-based supercapacitor with a wide operating potential window and high specific capacitance exhibits an ultrahigh volumetric energy density (51 $mWh\,cm^{-3}$) together with a high power density of 18 $W\,cm^{-3}$. The volumetric energy density is more than two times larger than the best values of aqueous and nonaqueous supercapacitors reported in the literature (Figure S7a).[1b,f,j,11,13a,18] Although the metal skeleton in the composite electrode is much heavier than carbon materials and the oxyhydroxide, the energy density of the cell based on the total mass of the two electrodes can still keep a high value of ca. 15 $Wh\,kg^{-1}$, comparable to the best mass energy density reported in the literature.[1b,f,j,11,13a,18a]

The electrochemical impedance spectroscopy (EIS) of the oxyhydroxide-based electrode was measured from 0.1 Hz to 100 kHz with the alternative current (ac) voltage amplitude of 10 mV. The resultant Nyquist plots are shown in Figure 4d. In the high-frequency region, the electrode shows a very small radius (R_{ct}) of the semicircle, indicating the low charge-transfer resistance at the electrode/electrolyte interface.[8a] The low intrinsic resistance of the multicomponent oxyhydroxide is most likely associated with the highly conductive metallic skeletons. In the low frequency region, the Warburg impedance (Z_W) demonstrates the high efficiency of the semi-infinite diffusion of cations in the bulk electrode. The cycling-life testing of the multicomponent oxyhydroxide-based supercapacitor was carried out by repeating the charge/discharge tests at a current density of 3 $A\,cm^{-3}$. Obvious capacitance degeneration cannot be seen during the cycling test and the retention ratio keeps as high as 99.7% after 2300 cycles (Figure S7b), demonstrating the excellent stability of the novel electrode material.

Although many pseudocapacitive materials are known to have a high theoretical capacitance, realization of the high capacitance for high-energy applications is often limited by their poor conductivity, narrow working potential window, and low electrochemical and mechanical stability.[1d,e] The NiCuMnOOH oxyhydroxide has a mixed-valence state and is supported by the highly conductive metal skeleton. Thus, it has high electrical conductivity for the full utilization of the high capacitance of the multicomponent oxyhydroxide from thick films. The high specific capacitance and wide working potential window also benefit from the multiple redox reactions at different potentials. Combining with the wide working potential window of 1.8 V, the oxyhydroxide based supercapacitor offers very high energy density, accompanied by the high power density. The findings of ultrahigh capacitive performance of the multicomponent mixed-valence oxyhydroxide in a wide working-potential window may open a new field of advanced pesudocapacitive materials for the next generation electrical energy storage.

Keywords: multicomponent oxides · nanoporous metals · oxyhydroxides · polarization · supercapacitors

How to cite: *Angew. Chem. Int. Ed.* **2015**, *54*, 8100–8104
Angew. Chem. **2015**, *127*, 8218–8222

[1] a) J. Yan, Q. Wang, T. Wei, Z. Fan, *Adv. Energy Mater.* **2014**, *4*, 1300816; b) Y. Gogotsi, P. Simon, *Science* **2011**, *334*, 917–918; c) W. Gu, G. Yushin, *Wiley Interdiscip. Rev. Nanomed. Nanobiotechnol.* **2014**, 424–473; d) G. Wang, L. Zhang, J. Zhang, *Chem. Soc. Rev.* **2012**, *41*, 797–828; e) P. Simon, Y. Gogotsi, *Nat. Mater.* **2008**, *7*, 845–854; f) Y. Zhu, S. Murali, M. D. Stoller, K. J. Ganesh, W. Cai, P. J. Ferreira, A. Pirkle, R. M. Wallace, K. A. Cychosz, M. Thommes, D. Su, E. A. Stach, R. S. Ruoff, *Science* **2011**, *332*, 1537–1541; g) X. Y. Lang, A. Hirata, T. Fujita, M. W. Chen, *Nat. Nanotechnol.* **2011**, *6*, 232–236; h) K. Naoi, S. Ishimoto, J. Miyamoto, W. Naoi, *Energy Environ. Sci.* **2012**, *5*, 9363–9373; i) M. F. L. De Volder, S. H. Tawfick, R. H. Baughman, A. J. Hart, *Science* **2013**, *339*, 535–539; j) M. F. El-Kady, V. Strong, S. Dubin, R. B. Kaner, *Science* **2012**, *335*, 1326–1330.

[2] R. L. LeRoy, C. T. Bowen, D. J. LeRoy, *J. Electrochem. Soc.* **1980**, *127*, 1954–1962.

[3] M. Armand, F. D. Endres, R. MacFarlane, H. Ohno, B. Scrosati, *Nat. Mater.* **2009**, *8*, 621 – 629.
[4] a) J. Erlebacher, M. J. Aziz, A. Karma, N. Dimitrov, K. Sieradzki, *Nature* **2001**, *410*, 450 – 453; b) J. Kang, A. Hirata, H.-J. Qiu, L. Chen, X. Ge, T. Fujita, M. Chen, *Adv. Mater.* **2014**, *26*, 269 – 272.
[5] a) M. Hasan, M. Jamal, K. M. Razeeb, *Electrochim. Acta* **2012**, *60*, 193 – 200; b) J. P. Liu, J. Jiang, M. Bosman, H. J. Fan, *J. Mater. Chem.* **2012**, *22*, 2419 – 2426.
[6] a) S. K. Shinde, D. P. Dubal, G. S. Ghodake, V. J. Fulari, *RSC Adv.* **2015**, *5*, 4443 – 4447; b) J. L. Kang, A. Hirata, L. Kang, X. Zhang, Y. Hou, L. Chen, C. Li, T. Fujita, K. Akagi, M. Chen, *Angew. Chem. Int. Ed.* **2013**, *52*, 1664 – 1667; *Angew. Chem.* **2013**, *125*, 1708 – 1711.
[7] a) C. Xu, H. Du, B. Li, F. Kang, Y. Zeng, *J. Electrochem. Soc.* **2009**, *156*, A435 – 441; b) Q. Lu, J. G. Chen, J. Q. Xiao, *Angew. Chem. Int. Ed.* **2013**, *52*, 1882 – 1889; *Angew. Chem.* **2013**, *125*, 1932 – 1940.
[8] a) H. Kim, N. Popov, *J. Electrochem. Soc.* **2003**, *150*, D56 – D62; b) K. Kinoshita, *Electrochemical oxygen technology*, 1st ed., Wiley, New York, **1992**.
[9] H. Y. Lee, J. B. Goodenough, *J. Solid State Chem.* **1999**, *148*, 81 – 84.
[10] C. Tessier, C. Faure, L. Guerlou-Demourgues, C. Denage, G. Nabias, C. Delmas, *J. Electrochem. Soc.* **2002**, *149*, A1136 – A1145.
[11] a) J. Yan, Z. Fan, W. Sun, G. Ning, T. Wei, Q. Zhang, R. Zhang, L. Zhi, F. Wei, *Adv. Funct. Mater.* **2012**, *22*, 2632 – 2641; b) X. Dong, Z. Guo, Y. Song, M. Hou, J. Wang, Y. Wang, Y. Xia, *Adv. Funct. Mater.* **2014**, *24*, 3405 – 3412.
[12] J. Wang, J. Polleux, J. Lim, B. Dunn, *J. Phys. Chem. C* **2007**, *111*, 14925 – 14931.
[13] a) A. E. Fischer, K. A. Pettigrew, D. R. Rolison, R. M. Stroud, J. W. Long, *Nano Lett.* **2007**, *7*, 281 – 286; b) H. C. Chien, W. Y. Cheng, Y. H. Wang, S. Y. Lu, *Adv. Funct. Mater.* **2012**, *22*, 5038 – 5043.
[14] M. Ghidiu, M. R. Lukatskaya, M. Zhao, Y. Gogotsi, M. W. Barsoun, *Nature* **2014**, *516*, 78 – 81.
[15] J. P. Zheng, P. J. Cygan, T. R. Jow, *J. Electrochem. Soc.* **1995**, *142*, 2699 – 2703.
[16] a) C. C. Hu, W. C. Chen, K. H. Chang, *J. Electrochem. Soc.* **2004**, *151*, A281 – A290; b) L. Y. Chen, Y. Hou, J. Kang, A. Hirata, T. Fujita, M. Chen, *Adv. Energy Mater.* **2013**, *3*, 851 – 856.
[17] M. Toupin, T. Brousse, D. Bélanger, *Chem. Mater.* **2004**, *16*, 3184 – 3190.
[18] a) F. H. Meng, Y. Ding, *Adv. Mater.* **2011**, *23*, 4098 – 4102; b) D. Pech, M. Brunet, H. Durou, P. Huang, V. Mochalin, Y. Gogotsi, P. L. Tabema, P. Simon, *Nat. Nanotechnol.* **2010**, *5*, 651 – 654.

Received: January 8, 2015
Revised: March 16, 2015
Published online: May 27, 2015

